IEEE Photonics Journal
An IEEE Photonics Society Publication

Open Access

Design of Hollow Core Bragg Fibers for a Compact Fluorescence Sensing Scheme

Volume 9, Number 2, April 2017

Liang Shang
Kunjie Zheng

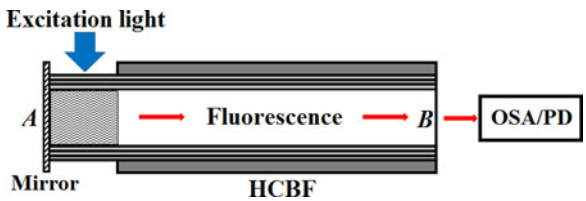

DOI: 10.1109/JPHOT.2017.2677582
1943-0655 © 2017 IEEE

IEEE photonics SOCIETY

IEEE

Design of Hollow Core Bragg Fibers for a Compact Fluorescence Sensing Scheme

Liang Shang and Kunjie Zheng

School of Physics and Engineering, Shandong Provincial Key Laboratory of Laser Polarization and Information Technology, Qufu Normal University, Qufu 273165 China

DOI:10.1109/JPHOT.2017.2677582

Manuscript received January 13, 2017; revised February 26, 2017; accepted February 28, 2017. Date of publication March 9, 2017; date of current version March 21, 2017. This work was supported in part by the National Natural Science Foundation of China under Grant 11404185 and in part by the Natural Science Foundation of Shandong Province of China under Grant ZR2013FQ012. Corresponding author: L. Shang (e-mail: shliang_sd@126.com).

Abstract: We propose a compact fluorescence sensing scheme based on hollow core Bragg fibers (HCBFs) that simultaneously serve as a sample cell, a collector, and a delivery channel for the desired fluorescence, as well as a filter for the residual excitation light mixed with fluorescence. The liquid samples filled in the air core are laterally irradiated by the excitation light for the spatial separation from fluorescence. Both the photonic bandgap (PBG) effect in the common HCBF (C-HCBF) and the transverse resonant behavior in the defect HCBF (D-HCBF) can be employed for filtering the residual excitation light mixed with fluorescence. The performance of the fluorescence sensing scheme strongly depends on the characteristics of PBG and modal loss for both types of HCBFs. According to the design principle, we present the design strategies of C-HCBF and D-HCBF for fluorescence sensing, respectively. Two typical examples are demonstrated to confirm the feasibility of our proposed fluorescence sensing scheme. We believe that our proposal would provide a new way to build a compact fluorescence sensing system.

Index Terms: Microstructured fibers, hollow core Bragg fiber, fluorescence sensing.

1. Introduction

Fluorescence sensing is an attractive detection technique for qualitative or quantitative chemical and biological analysis. Due to its merits of high sensitivity, strong selectivity, and wide dynamic range, fluorescence sensing technique has great potential for applications in medicine, biochemistry, environmental monitoring, and food security [1], [2]. Therefore, it is urgently needed to build a compact and highly sensitive fluorescence sensing system. In recent years, the substitutions of laser diodes (LDs) and light emitting diodes (LEDs) for bulky lamps and solid-state lasers as excitation sources partly contribute to miniaturizing fluorescence sensors [3]–[5]. Further, various fiber-type waveguides with small size and flexibility also play a significant role in simplifying fluorescence detection systems.

To avoid using bulky coupling devices, multimode silica fibers were placed closely against samples for directly delivering excitation light or collecting fluorescence [6]. However, the fluorescence capture efficiency is restricted by the numerical aperture, and the detection sensitivity is limited by the large background noise originating from silica cores. For these reasons, a hollow core photonic crystal fiber (HCPCF) probe was proposed for highly sensitive fluorescence sensing, in which a

polystyrene microsphere was used for coupling of excitation light and fluorescence [7]. In fact, HCPCF can simultaneously act as a sample cell, a delivery channel for excitation light, and a collector for fluorescence. The excitation light directly irradiates liquid samples previously injected into the hollow core using selective-filling technique, and then the generated fluorescence propagates in the core relying on photonic bandgap (PBG) effect [8]. In addition, samples can be filled into the holey cladding and interact with excitation light via the evanescent field [9]. Similarly, microstructured silica and polymer fibers were also employed for fluorescence sensing [10], [11], in which samples in air holes were excited by the evanescent field of excitation light, and the emitted fluorescence could be guided either in the cladding or in the core. However, it was experimentally demonstrated that HCPCFs are more suitable for highly sensitive fluorescence detection than microstructured fibers relying on evanescent-field effect [12]. To enhance the sensitivity of evanescent-field-based detection, several types of suspended core microstructured fibers were proposed [5], [13]. Recently, liquid core waveguides (LCWs) based on glass and polymer capillaries were widely employed in microfluidic capillary electrophoresis analysis for fluorescence detection [3], [14], [15]. Generally, liquid samples were irradiated by the excitation light passing through the lateral wall of LCWs, and the collected fluorescence was trapped in the liquid core with the aid of total internal reflection (TIR). Thus, the excitation light and fluorescence can be separated spatially without dichroic mirrors. However, in most of the existing fluorescence sensing schemes, discrete filters or monochromators were still required to eliminate the residual excitation light mixed with fluorescence for improving signal to noise ratio (SNR). In particular, the LCW needs to be packaged in a lightproof tube for shielding background light [15]. Thus, we are motivated by the aforementioned issues to further simplify the fluorescence sensing schemes.

Hollow core Bragg fibers (HCBFs), regarded as a special class of PBG fibers, can guide light in an air core using one-dimensional PBG (1DPBG) effect [16]. With an omnidirectional reflecting cladding, HCBFs can strongly confine light from all incidence angles and polarizations in the core [17]. As a result of their novel guiding mechanism and excellent transmission performance, HCBFs have attracted increasing interest in the fields of trace-gas detection and biochemical sensing [18]–[26]. A conventional HCBF intrinsically has the characteristic of wideband band-pass filter due to the PBG effect. On the other hand, with a defect layer introduced into a common cladding, the HCBF would perform narrow band-rejection filtering as a result of the transverse resonant (TR) behavior [27]. Thus, HCBFs have great potential for further miniaturizing the fluorescence detection system, because of their ability as a filter to replace bulky filters or monochromators in conventional systems. Moreover, because the multilayer claddings of HCBFs are generally formed by solid materials (except for all-silica and polymer ones [20], [28]), the sophisticated pretreatment of cladding holes in HCPCFs (e.g., selective-filling treatment [8]) before injecting liquid analyte into the hollow core is needless. Unlike LCWs based on TIR, light still can be guided in the liquid-filled core of an HCBF even with lower refractive index than that of the cladding. All the performance characteristics mentioned above show that HCBFs are more suitable than HCPCFs and LCWs for building a compact fluorescence sensing system.

In the present paper, we propose a compact fluorescence sensing scheme based on HCBFs. Both the PBG effect and the TR behavior are used as the filtering mechanism for the residual excitation light mixed with fluorescence. According to the design principle and strategies, two typical design examples are presented to validate the feasibility of our proposed fluorescence sensing scheme.

2. Model and Method

2.1 Theoretical Model

Fig. 1(a) schematically shows the cross section of a common HCBF (C-HCBF). A hollow core with the refractive index of n_c and diameter of d_c is coaxially surrounded by a common 1-D periodic cladding (1DPC) composed of alternating layers with high and low refractive indices (denoted by n_h and n_l, respectively). The high-index layers with thickness of t_h are marked in black, and the low-index layers with thickness of t_l are marked in light gray. The cladding period of Λ is the sum of t_h and t_l. For a fixed Λ, t_h and t_l are determined by the quarter-wave stack condition at glancing incidence

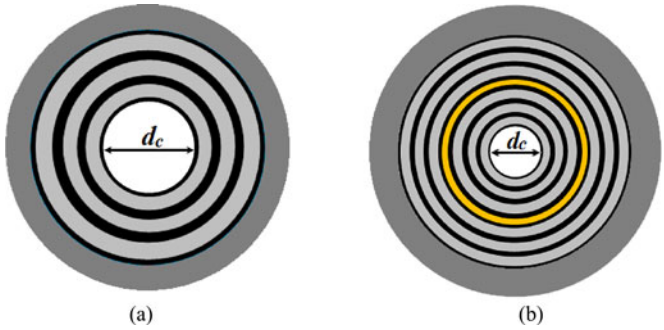

Fig. 1. Schematic cross sections of (a) C-HCBF and (b) D-HCBF. The high and low refractive index layers are marked in black and light gray, respectively. The dark gray areas indicates the protective layers. The yellow layer in (b) is the low-index defect layer.

($t_h/t_l = \sqrt{n_l^2 - 1}/\sqrt{n_h^2 - 1}$ [29]). Notably, the thicknesses of the innermost and outermost high-index layers are $t_h/2$ for suppressing surface modes [30]. The outermost dark gray area represents a protective thick layer with the same refractive index as n_l.

The introduction of a defect layer into a common 1DPC can be realized by varying the thickness of a high-index or low-index layer, or by adding a layer with another material. In practice, if the defect layer is made of a different material, it is difficult to make its optical, thermal, and mechanical properties compatible with those of high-index and low-index layers. Thus, for simplicity, here the transverse resonant structure is formed by introducing a defect layer with a thickness of t_d and a refractive index of $n_d = n_l$, as shown in Fig. 1(b). The TR behavior is induced by the interaction between guided modes and defect modes, which would influence the dispersion and loss characteristics of guided modes [27], [31], [32]. Accordingly, the transmission spectra of an HCBF with a defect layer (D-HCBF) show the evident performance of band-rejection filtering. The central wavelength of such a band-rejection filter (i.e., the resonant wavelength of defect modes) based on the D-HCBF is determined by both the thickness and location of the defect layer [27].

Considering that the As_2S_3 with high-index and polyetherimide (PEI) with low-index have been successfully employed for HCBFs in the targeted visible band [19], [30], in the following sections we will carry out the simulations for both types of HCBFs using this material combination. With the exclusion of material dispersion, their refractive indices are set to be $n_h = 2.582$ and $n_l = 1.685$, respectively [19].

2.2 Simulation Method

As demonstrated in our previous work, we calculate the PBG structure of HCBFs using the transfer matrix method (TMM) [33]. The coaxial cladding of a C-HCBF can be regarded as a group of ternary unit cells. The characteristic matrix for the jth unit cell is given by

$$M_j = \begin{bmatrix} \cos\delta_h & -\frac{i}{\eta_h}\sin\delta_h \\ -i\eta_h \sin\delta_h & \cos\delta_h \end{bmatrix} \begin{bmatrix} \cos\delta_l & -\frac{i}{\eta_l}\sin\delta_l \\ -i\eta_l \sin\delta_l & \cos\delta_l \end{bmatrix} \begin{bmatrix} \cos\delta_h & -\frac{i}{\eta_h}\sin\delta_h \\ -i\eta_h \sin\delta_h & \cos\delta_h \end{bmatrix} \quad (1)$$

where $\delta_h = \pi n_h t_h \cos\theta_h/\lambda$ and $\delta_l = 2\pi n_l t_l \cos\theta_l/\lambda$. $\eta_q = n_q \cos\theta_q$ and $\eta_q = n_q/\cos\theta_q$ are for the transverse electric (TE) and transverse magnetic (TM) waves, respectively, and q represents h or l. θ_h and θ_l denote the incidence angles in the high-index and low-index layers, respectively. λ is the free space wavelength.

The total characteristic matrix of M for the cladding of a C-HCBF can be written as

$$M = \prod_{j=1}^{N} M_j \quad (2)$$

where N is the period number. Similarly, given that the low-index defect is inserted into the N_dth unit cell, the total characteristic matrix of M for the cladding of a D-HCBF can be written as

$$M = \left(\prod_{j=1}^{N_d-1} M_j\right) M_{N_d} \left(\prod_{j=N_d+1}^{N} M_j\right). \tag{3}$$

In (3), the characteristic matrix of M_{N_d} is given by

$$M_{N_d} = \begin{bmatrix} \cos\delta_h & -\frac{i}{\eta_h}\sin\delta_h \\ -i\eta_h \sin\delta_h & \cos\delta_h \end{bmatrix} \begin{bmatrix} \cos\delta_d & -\frac{i}{\eta_d}\sin\delta_d \\ -i\eta_d \sin\delta_d & \cos\delta_d \end{bmatrix} \begin{bmatrix} \cos\delta_h & -\frac{i}{\eta_h}\sin\delta_h \\ -i\eta_h \sin\delta_h & \cos\delta_h \end{bmatrix} \tag{4}$$

where $\delta_d = 2\pi n_l t_d \cos\theta_d/\lambda$. $\eta_d = n_l \cos\theta_d$ and $\eta_d = n_l/\cos\theta_d$ are for the TE and TM waves, respectively. θ_d is the incidence angles in the defect layer.

For an incidence angle of θ_{in} in the air core, the reflectivity of $R_{s,p}(\theta_{in})$ from the coaxial cladding can be expressed as

$$R_{s,p}(\theta_{in}) = \left|\frac{(m_{11} + \eta_{out}m_{12})\eta_{core} - (m_{21} + \eta_{out}m_{22})}{(m_{11} + \eta_{out}m_{12})\eta_{core} + (m_{21} + \eta_{out}m_{22})}\right|^2 \tag{5}$$

where s and p represent the TE and TM waves, respectively. m_{11}, m_{12}, m_{21}, and m_{22} are the elements of M. $\eta_{core} = n_c \cos\theta_{in}$ and $\eta_{out} = n_l \cos\theta_{out}$ are for the TE waves, while $\eta_{core} = n_c/\cos\theta_{in}$ and $\eta_{out} = n_l/\cos\theta_{out}$ are for the TM waves, where θ_{out} is the refraction angle in the outermost layer. For a given incidence angle, the relation between the reflectivity and wavelength can be achieved from (5). Then the PBG is determined by the wavelength range for the reflectivity not less than 99% [34].

The transmission loss characteristics of both C-HCBF and D-HCBF are also very important for demonstrating our proposed HCBF-based fluorescence sensing scheme. Similarly to the previous works [20], [24], we focus our attention on the predominant confinement losses (CLs) of both types of HCBFs, which can be calculated by the ray-optics method (ROM). Although it cannot provide the dispersion relations and modal distributions of both core and defect modes, the ROM has advantages of much higher calculating speed and more reduced memory consumption over the finite difference time domain method and finite element method (FEM), and thereby is more suitable for rapid analysis and design of large-core HCBFs [35]. Based on the ROM, the CL is given by [36]

$$CL = 4.34\frac{1 - R(\theta_z)}{d_c \tan(\theta_z)} \ (\text{dB/m}) \tag{6}$$

where $\theta_z = \cos^{-1}(\lambda U_{mn}/(\pi d_c n_c))$, and U_{mn} is the n-th root of the (m-1) order of Bessel function. $R(\theta_z) = R_s(\theta_z)$ and $R(\theta_z) = R_p(\theta_z)$ are for the pure TE and TM modes with $m = 0$, respectively. $R(\theta_z) = [R_s(\theta_z) + R_p(\theta_z)]/2$ is for the mixed modes with $m \neq 0$.

3. Configuration and Design Principle

Fig. 2 shows the schematic configuration of the HCBF-based fluorescence sensing scheme. The liquid analyte containing fluorescent substance is injected into port *A* of the hollow core of an HCBF (C-HCBF or D-HCBF) using capillary action. The injected solution expands several centimeters in the axial direction, which is indicated by the shaded area. The output end of an excitation light source lies so closely against the lateral surface of the HCBF that the excitation light can pass through the multilayer cladding and stimulate the fluorescent solution. To ensure more excitation light entering the liquid-filled core, it is better to strip the protective layer by using etching techniques (e.g., wet chemical etching or reactive ion etching [37]) in advance. Notably, this pretreatment is not necessary, because the excitation light still can be injected into the core even with the protective layer. When its wavelength is within the PBG range, the generated fluorescence can be well confined in the core, and then it can propagate along the fiber axis until the distal end (port *B* shown in Fig. 2) connecting a photodetector (PD) or an optical spectrum analyzer (OSA). To collect more forward

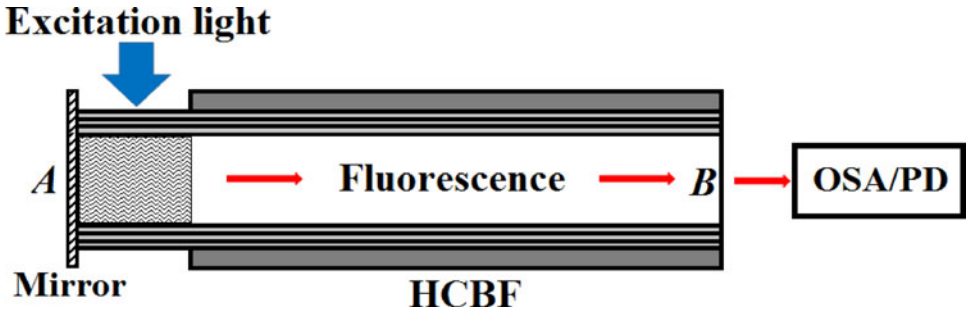

Fig. 2. Schematic configuration of HCBF-based fluorescence sensing scheme.

fluorescence at port *B*, a mirror is placed at port *A* to reflect the backward fluorescence back into the core. As can be seen from Fig. 2, the orthogonality in directions guarantees the spatial separation of the excitation light from the fluorescence. Notably, in contrast with sensing schemes based on hollow core waveguides, our proposed fluorescence sensing scheme is more compact due to the lack of bulky devices for filtering the residual excitation light. This structural difference is attributed to the fact that both the C-HCBF based on the PBG effect and the D-HCBF based on the TR behavior can serve as an inline fiber filter. In addition, in contrast with noise cancellation requirements for LCWs, special preventive measures against the noisy background light are not needed for both types of HCBFs, because they have thick non-transparent claddings.

Generally speaking, in our proposed fluorescence sensing scheme, both the C-HCBF and D-HCBF can simultaneously serve as a sample cell, a collector and a delivery channel for the desired fluorescence, and a filter for the residual excitation light. Consequently, the performance of such a scheme strongly depends on the transmission characteristics of both types of HCBFs. More specifically, for compact and highly sensitive fluorescence sensing, the structural parameters of HCBFs should be optimally designed to enable their PBG and modal loss characteristics to meet the four requirements listed below.

First, to ensure that more excitation light can favorably penetrate the multilayer cladding of HCBFs and interact with the fluorescent substance, the excitation wavelength (denoted by λ_E) should fall outside of the PBG range at normal incidence. Here, for simplicity, it is assumed that the excitation light is normally incident on the lateral surface of the cladding. Notably, this assumption would be accurate for LDs with a very small divergent angle but might bring some errors for LEDs with the divergent angle of dozens of degrees.

Second, to enhance the capture efficiency for the chaotic fluorescence in various directions and to reduce the transmission loss, the fluorescence wavelength (denoted by λ_F) should fall within the omnidirectional PBG (OPBG) range of HCBFs.

Third, given that the wavelength interval between excitation light and fluorescence is large enough, λ_E should fall outside of the PBG ranges for both TE and TM waves at glancing incidence, or at least lie at both PBG edges. Under these conditions, the excitation light would have much higher loss than the fluorescence because of the PBG effect so that the residual excitation light mixed with the desired fluorescence would gradually disappear in a C-HCBF before getting to port *B*.

Fourth, given that the wavelength interval between excitation light and fluorescence is small, the TR behavior needs to be used for filtering the residual excitation light, in which λ_E should be consistent with the resonant wavelength. Under this condition, the noisy excitation light would suffer from a sharp increase in losses and thereby be lost during the forward transmission in a D-HCBF.

The first and second conditions are essential for coupling the excitation light, and collecting and delivering the fluorescence, respectively. The third and fourth conditions are crucial for C-HCBF serving as a band-pass filter and for D-HCBF serving as a band-rejection filter, respectively. It is well known from the literature that high sensitivity can be achieved primarily by enhancing the interaction of excitation light with fluorescent substance [12], [13], by increasing the fluorescence

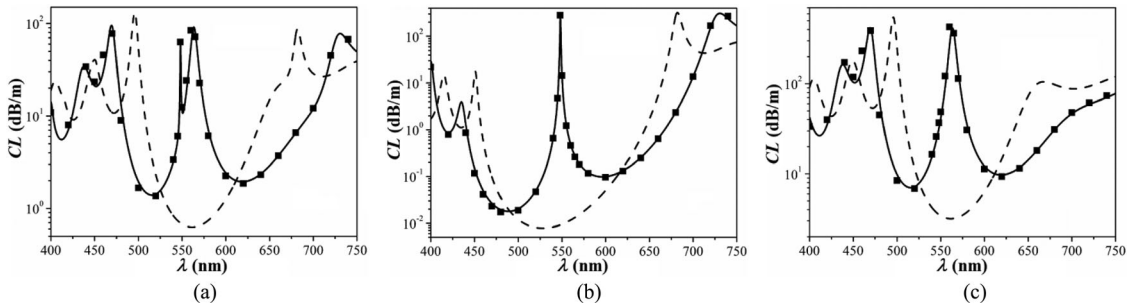

Fig. 3. Loss spectra of (a) HE_{11}, (b) TE_{01}, and (c) TM_{01} modes. The solid and dashed lines represent CL calculated by ROM for D-HCBF and C-HCBF, respectively. The solid squares represent CL calculated by FEM for D-HCBF.

capture efficiency [7], [12], [13], and by reducing the disturbance of noisy signals including residual excitation light mixed with fluorescence [5], [12], [14]. Therefore, the presented four requirements for HCBFs are potentially useful for improving the sensitivity. For a given material combination of claddings, the PBG structure of the HCBF is determined by the thicknesses of high-index and low-index layers. Consequently, the adjustment of PBG ranges can be conveniently realized by varying the values of t_h and t_l. However, the influence of the defect layer on the modal loss characteristics still deserves further discussion, as the foundation for filtering in the D-HCBF-based fluorescence sensing scheme.

4. Band-Rejection Filtering Characteristics

The confinement loss of the fundamental HE_{11} mode depends on both TE and TM components, of which the latter is dominant. Thus, in contrast to the previous work that considered TE_{01} mode [27], here we focus on the loss evolution of the much more representative HE_{11} mode with the defect layer in a D-HCBF. Fig. 3(a) shows the loss spectrum of the HE_{11} mode in a D-HCBF with $d_c = 60$ μm, $\Lambda = 160$ nm, $t_d = 2t_l$, $N_d = 3$, and $N = 7$. For comparison, the loss spectrum of the HE_{11} mode in a C-HCBF with $d_c = 60$ μm, $\Lambda = 160$ nm, and $N = 7$ is also shown in Fig. 3(a). As we can see from this figure, the introduction of the defect layer gives rise to a wide loss peak at 563.4 nm and a narrow one at 548.2 nm in the low-loss transmission window of the HE_{11} mode. According to the bandwidth of loss peaks, we define the wide one as the main peak (MP), and the narrow one as the secondary peak (SP). This result is quite different from that obtained for the TE_{01} mode, in which case only one loss peak exists [27]. To validate the correctness of simulation results calculated by the ROM, we recalculate the confinement losses using the FEM as shown in Fig. 3(a), which indicating a good agreement between them.

The modal loss characteristics of the mixed HE_{11} mode is essentially determined by the reflection characteristics of TE and TM waves from the coaxial cladding of the D-HCBF. To understand the reasons for the emergence of MP and SP mentioned above, we plot the reflectivity as a function of wavelength for TE and TM waves at the characterized incidence angle of $\theta_z = 89.6^\circ$ in Fig. 4. It can be seen that two reflectivity dips (*A* and *B*) with central wavelengths of 548.2 nm and 563.4 nm occur for TE and TM waves, respectively. Compared with the loss spectrum of the HE_{11} mode (dashed line), the central wavelength of SP (denoted by λ_{SP}) is identical to that of dip *A* for TE waves, and the central wavelength of MP (denoted by λ_{MP}) is identical to that of dip *B* for TM waves. In fact, the dependence of MP on the reflection characteristic of the TM waves is attributed to the dominant influence of TM components on the transmission of the HE_{11} mode [29]. For further illustration, the loss spectra of the TE_{01} and TM_{01} modes in the D-HCBF are also shown in Fig. 3(b) and (c), respectively. The TE_{01} mode, as well as the TM_{01} mode, has just one loss peak, which agrees well with that shown in [27]. In addition, the central wavelengths of the TE_{01} and TM_{01} modes are the

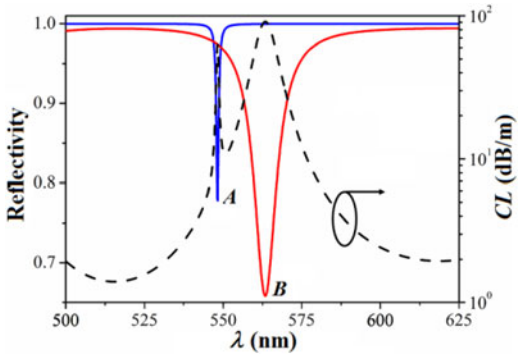

Fig. 4. Reflectivity as a function of wavelength for TE (blue) and TM (red) waves at $\theta_z = 89.6^\circ$ in D-HCBF. The dashed line represents the loss spectrum of HE_{11} mode.

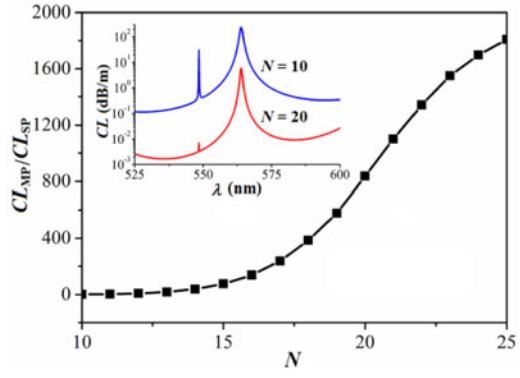

Fig. 5. Ratio of CL_{MP}/CL_{SP} as a function of N in D-HCBF. (Inset) Loss spectra of HE_{11} mode for $N = 10$ and $N = 20$.

same as those of dip *A* and *B*, respectively, due to the fact that the transmission characteristics of pure TE or TM modes are solely dependent on the reflections of TE or TM waves, respectively.

The confinement losses of guided modes can be reduced effectively by increasing N, as a result of the enhancement of reflectivity for TE and TM waves from the multilayer cladding. However, the influence of N on the reflectivity enhancement for TE waves is different from that for TM waves. Fig. 5 shows the ratio between the loss values of MP and SP (denoted by CL_{MP} and CL_{SP}, respectively) as a function of N in a D-HCBF with $d_c = 60\ \mu$ m, $\Lambda = 160$ nm, $t_d = 2t_l$, and $N_d = 3$. As can be seen from this figure, the ratio of CL_{MP}/CL_{SP} increases with increasing N for a given N_d, and the slope of the curve initially increases and then decreases with N. The increase of ratio with N is approximately linear for N ranging from 18 to 23. Thus, we can conclude that the influence of increasing N on the reflectivity enhancement is stronger for TE waves than for TM waves, indicating that the SP of the HE_{11} mode would be effectively suppressed by increasing N. As shown in the inset in Fig. 5, the SP is significantly reduced for $N = 20$, compared with its value for $N = 10$. Notably, both λ_{MP} and λ_{SP} do not change with N for a given N_d.

Fig. 6 shows the loss spectra of the HE_{11} mode for different diameters of d_c in a D-HCBF with $\Lambda = 160$ nm, $t_d = 2t_l$, $N_d = 3$, and $N = 12$. It can be seen that the variation of d_c has little influence on the ratio of CL_{MP}/CL_{SP}, despite the decreased confinement loss of the HE_{11} mode with increasing d_c. Additionally, both λ_{MP} and λ_{SP} do not change with d_c, but it is evident that the bandwidth of the MP decreases with increasing d_c.

According to the design principle mentioned in Section 3, the loss peak would be used for filtering the residual excitation light and the longer wavelength range with low transmission loss would be used for delivering the desired fluorescence. Therefore, the improvement of SNR strongly

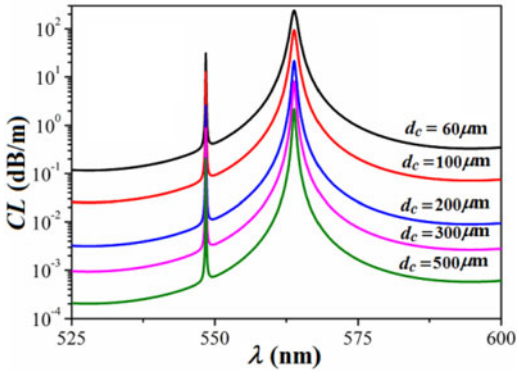

Fig. 6. Loss spectra of HE_{11} mode for different values of d_c in D-HCBF.

TABLE 1
Ratios of $C = CL_{MP}/CL_{\min}$ for Different Values of N

N	CL_{MP}(dB/m)	$CL_{\min}$(dB/m)	C
10	242.13	0.71	341.0
12	237.70	0.33	720.3
15	85.45	9.36×10^{-2}	912.9
20	5.94	9.25×10^{-3}	642.2
25	0.35	7.94×10^{-4}	440.8

TABLE 2
Ratios of $C = CL_{MP}/CL_{\min}$ for Different Values of d_c

d_c (μm)	CL_{MP}(dB/m)	$CL_{\min}$(dB/m)	C
60	237.70	0.33	720.3
100	93.37	7.16×10^{-2}	1304.1
200	21.39	8.95×10^{-3}	2389.9
300	8.15	2.65×10^{-3}	3075.5
500	2.21	5.73×10^{-4}	3856.9

depends on increasing the difference between the peak loss for excitation light and the lower loss for fluorescence. To quantify this contrast, we resort to the ratio of $C = CL_{MP}/CL_{\min}$, where $CL_{\min}$ is the minimum loss in the longer range than the MP. The reason for selecting CL_{MP} for this ratio rather than CL_{SP} is that most guided modes including the pure TM and mix modes would suffer from great transmission losses at λ_{MP}. As we can see from Figs. 5 and 6, λ_{MP} cannot be changed by varying N and d_c. However, the values of C listed in Tables 1 and 2 can be changed by using both methods, respectively. We can see that the values of C initially increase and then decrease with

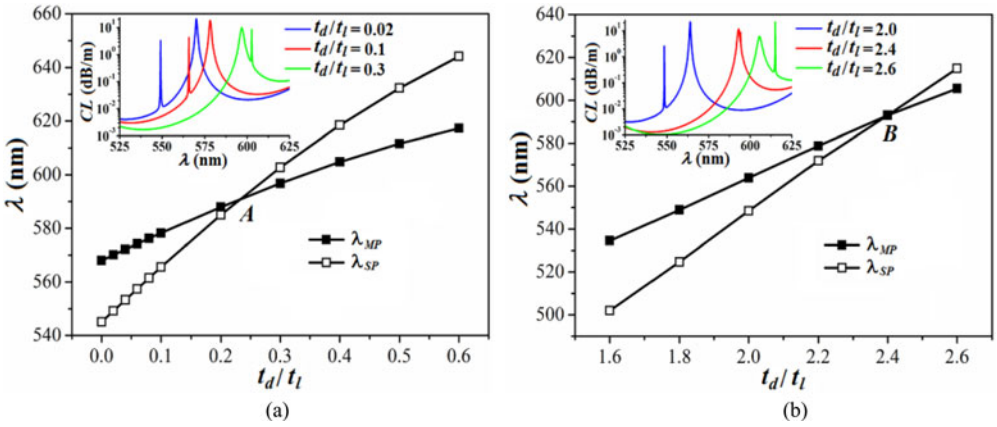

Fig. 7. λ_{MP} and λ_{SP} as a function of t_d/t_l for (a) $0 \leq t_d/t_l < 1$ and (b) $t_d/t_l > 1$. (Insets in (a) and (b)) Loss spectra of HE_{11} mode for different values of t_d/t_l.

increasing N, indicating that an optimum value of N exists for the maximum value of C. In contrast, the values of C increase monotonously with increasing d_c.

Next, we will examine the influence of thickness of the defect layer on the loss characteristics of the HE_{11} mode. Fig. 7(a) shows λ_{MP} and λ_{SP} as a function of t_d/t_l in a D-HCBF with $d_c = 200$ μm, $\Lambda = 160$ nm, $N_d = 3$, and $N = 12$ for $0 \leq t_d/t_l < 1$. From this figure, we can see the red-shifts in both λ_{MP} and λ_{SP} with increasing t_d at different growth rates, and both curves intersect at point A. On the left of point A, λ_{MP} is longer than λ_{SP}, and the difference between them decreases with increasing t_d. In contrast, on the right of point A, λ_{MP} is shorter than λ_{SP}, and the difference between them increases with increasing t_d. The intersection of both curves indicates the agreement between λ_{MP} determined by TM reflections and λ_{SP} determined by TE reflections. In this case, all the pure TE and TM modes, and mixed modes with the approximate θ_z would have high transmission loss at the same wavelength. Such a result has great practical significance for designing the HCBF-based fluorescence sensing system. Because both C-HCBF and D-HCBF used for fluorescence sensing are the large-core multimode fibers, their modal content is sophisticated for the residual excitation light transmitting in the air core. Although most higher-order modes can easily be filtered due to their huge losses [29], a few lower-order modes with similar θ_z (very close to 90° in the large core) can survive. To overcome this complexity, the matching condition of $\lambda_{MP} = \lambda_{SP}$ should be satisfied. Note that two neighboring high-index layers with the thickness of t_h can be regarded as a high-index defect layer with the thickness of $2t_h$, which is shown in Fig. 7(a) in the case of $t_d = 0$. It can be seen that the high-index defect layer can also induce the TR behavior, which is no longer detailed.

Fig. 7(b) shows λ_{MP} and λ_{SP} as a function of t_d/t_l in a D-HCBF with $d_c = 200$ μm, $\Lambda = 160$ nm, $N_d = 3$, and $N = 12$ for $t_d/t_l > 1$. Similar to those shown in Fig. 7(a), both curves intersect at point B. Although the values of t_d at points A and B are quite different, the corresponding wavelengths at both points are close to each other.

It has been known from Fig. 5 that both λ_{MP} and λ_{SP} do not vary with N for a given N_d, but the influence of N_d on both λ_{MP} and λ_{SP} for a given N is still worthy of discussion. Fig. 8 shows the variation of λ_{MP} and λ_{SP} with N_d ranging from 2 to 8 in a D-HCBF with $d_c = 200$ μm, $\Lambda = 160$ nm, $t_d = 2t_l$, and $N = 12$. The blue-shift in λ_{MP} and red-shift in λ_{SP} with increasing N_d can be observed from this figure. The difference between λ_{MP} and λ_{SP} gradually decreases to 0 with increasing N_d to 8. Moreover, λ_{MP} is always identical to λ_{SP} when $N_d \geq 8$. Notably, both the blue-shift of λ_{MP} and red-shift of λ_{SP} are weakened with increasing N_d, resulting from the weaker influence on the transmission characteristics of guide modes induced by the defect layer far away from the core. On the other hand, we can see from the inset in Fig. 8 that the bandwidth of the MP increases with increasing N_d, even when the defect layer moves further away from the core (for $N_d > 8$).

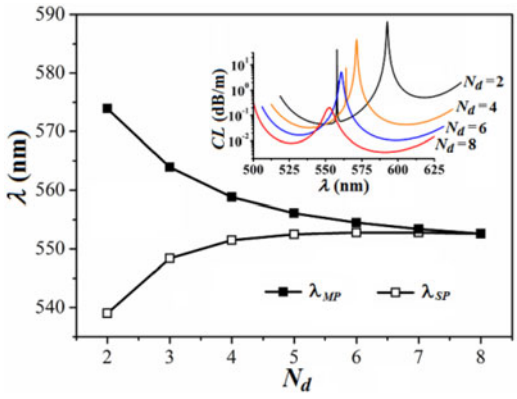

Fig. 8. λ_{MP} and λ_{SP} as a function of N_d. (Inset) Loss spectra of HE_{11} mode for different values of N_d.

TABLE 3
Ratios of $C = CL_{MP}/CL_{\min}$ for Different Values of N_d

N_d	CL_{MP}(dB/m)	$CL_{\min}$(dB/m)	C
2	23.47	2.35×10^{-2}	998.7
3	21.39	8.95×10^{-3}	2389.9
4	12.75	5.57×10^{-3}	2289.0
5	5.36	4.32×10^{-3}	1240.7
6	1.89	3.78×10^{-3}	500.0
7	0.62	3.57×10^{-3}	173.7
8	0.21	3.54×10^{-3}	59.3
9	6.45×10^{-2}	3.62×10^{-3}	17.8

We can conclude from Figs. 7 and 8 that the agreement of λ_{MP} and λ_{SP} could be realized by optimizing the value of d_c or N_d, but the results from both methods are distinguishable. As shown in Fig. 7(a) and (b), when $\lambda_{MP} = \lambda_{SP}$, both wavelengths corresponding to $CL_{\min}$ (around 615 nm) are outside of the OPBG ranging from 567 to 611 nm. In contrast, as shown in Fig. 8, the wavelength corresponding to $CL_{\min}$ (around 592 nm) is well within the OPBG range in the case of $\lambda_{MP} = \lambda_{SP}$. According to the second condition of the design principle mentioned in Section 3, the optimization of N_d for $\lambda_{MP} = \lambda_{SP}$ is preferred to that of d_c. However, as listed in Table 3, the ratio of $C = CL_{MP}/CL_{\min}$ decreases with increasing N_d ($N_d > 2$), indicating that the realization of $\lambda_{MP} = \lambda_{SP}$ in this case would be at the cost of decreasing the SNR.

Most notably, once λ_{MP} agrees with λ_{SP} by using those two approaches for the given values of t_h/t_l and t_d/t_l, both wavelengths would constantly stay the same for any value of Λ. Similar to the PBG, the same peak wavelength can also scale up with Λ, which is a significant rule for the design of D-HCBF-based band-rejection filter with different central wavelengths.

5. Design Examples for Fluorescence Sensing

In the visible range, the material dispersion of As_2S_3 and PEI cannot be neglected [19], which is a key issue in practical design of HCBFs. Based on the curves shown in [19], the refractive indices of As_2S_3 and PEI as a function of wavelength ranging from 400 to 800 nm are, respectively, expressed

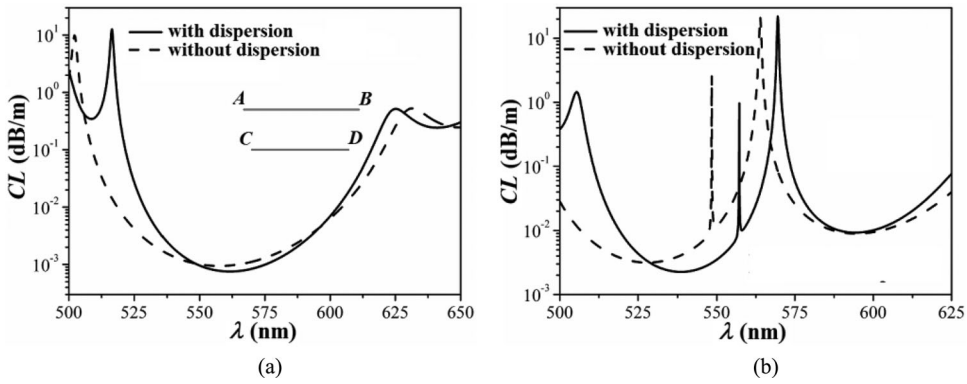

Fig. 9. Influence of material dispersion on loss spectra of HE_{11} mode in (a) C-HCBF and (b) D-HCBF. The line segments *AB* and *CD* in (a) represent OPBG ranges.

as

$$n_h = A_6\lambda^6 + A_5\lambda^5 + A_4\lambda^4 + A_3\lambda^3 + A_2\lambda^2 + A_1\lambda + A_0 \tag{7}$$

$$n_l = B_6\lambda^6 + B_5\lambda^5 + B_4\lambda^4 + B_3\lambda^3 + B_2\lambda^2 + B_1\lambda + B_0 \tag{8}$$

where $A_6 = -715.3139$, $A_5 = 2959.327$, $A_4 = -5032.7481$, $A_3 = 4493.2988$, $A_2 = -2213.3755$, $A_1 = 566.6904$, and $A_0 = -55.6705$; $B_6 = 75.1822$, $B_5 = -298.4697$, $B_4 = 486.5028$, $B_3 = -417.7243$, $B_2 = 200.3676$, $B_1 = -51.495$ and $B_0 = 7.3312$. In (7) and (8), λ is in microns.

Fig. 9(a) shows the influence of material dispersion on the loss spectra of HE_{11} mode in a C-HCBF with $d_c = 200$ μm, $\Lambda = 160$ nm, and $N = 12$. The low-loss transmission window for the HE_{11} mode becomes narrower as a result of including material dispersion, which is attributed to the PBG narrowing induced by the material dispersion [19]. As can be seen from Fig. 9(a), the original OPBG ranging from 567 to 611 nm (indicated by the line segment *AB*) decreases to that ranging from 570 to 607 nm (indicated by the line segment *CD*) with the material dispersion included. In both cases, the OPBG is regarded as the overlapped wavelength range in the reflectivity spectra of TM waves at $\theta_{in} = 0^\circ$ and $\theta_{in} = 85^\circ$, which was illustrated in [33]. As shown in Fig. 9(b), a similar comparison of loss spectra of the HE_{11} mode is carried out for a D-HCBF with $d_c = 200$ μm, $\Lambda = 160$ nm, $t_d = 2t_l$, $N_d = 3$, and $N = 12$. The influence of material dispersion results in red-shifts for both λ_{MP} and λ_{SP}, with shifts of 5.6 nm and 8.8 nm, respectively. In addition, the usable low-loss transmission range on the right of the loss peaks is also narrowed when the material dispersion is included. Thus, in the practical design of both C-HCBFs and D-HCBFs for fluorescence sensing, it is required to consider the influence of material dispersion on the PBG structure and the transmission characteristic of guided modes.

In accordance with the design principles established in Section 3, we present the design strategies using both C-HCBFs and D-HCBFs for a compact fluorescence sensing scheme. Further, we demonstrate the useful design examples for both types of HCBFs in two practical cases of fluorescence sensing.

The design strategy of C-HCBFs for fluorescence sensing is as follows: First, an initial value of Λ is determined by the agreement of central wavelengths for the fluorescence and OPBG, with the resulting value defined as Λ_i. Second, check whether λ_E is outside of the PBG range at normal incidence, and simultaneously is outside or at least on the edge of the PBG range at glancing incidence for both TE and TM waves. If these criteria are satisfied, the initial Λ_i can be set as the final value of Λ. Otherwise, the initial Λ_i needs to be finely adjusted using the rule of PBG structure scaling up with Λ, until the criteria are satisfied.

As demonstrated experimentally in [5], when the rhodamine 6G solution is excited by an LD with the central wavelength of 452 nm, the excited fluorescence has a central wavelength of 575 nm. In view of the large wavelength interval between the excitation light and fluorescence, we demonstrate

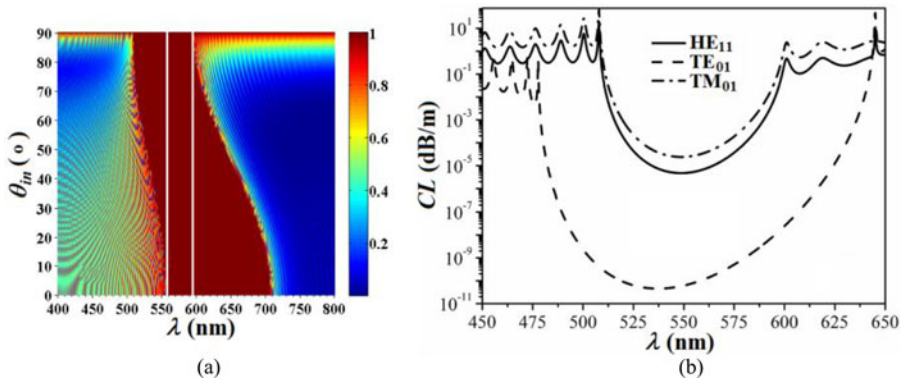

Fig. 10. (a) Reflectivity spectrum as a function of wavelength and incidence angle for TM waves and (b) loss spectra of HE_{11}, TE_{01} and TM_{01} modes in the designed C-HCBF with $d_c = 200$ μm, $\Lambda = 156$ nm, and $N = 20$.

a designed C-HCBF with $d_c = 200$ μm, $\Lambda = 156$ nm, and $N = 20$. Fig. 10(a) shows the reflectivity spectrum as a function of the wavelength and incidence angle for TM waves in the designed C-HCBF. As marked by the pair of white lines, the OPBG ranges from 558 to 595 nm, with the central wavelength at 576.5 nm, which is slightly longer than the targeted 575 nm due to the material dispersion. It can be seen from Fig. 10(a) that λ_E is well outside of both the PBG at normal incidence (558 to 706 nm) and the PBG for TE and TM waves at glancing incidence (480 to 644 nm and 510 to 595 nm, respectively). The loss spectra of the HE_{11}, TE_{01} and TM_{01} modes are shown in Fig. 10(b), whose confinement losses at 575 nm are 3.68×10^{-5} dB/m, 5.02×10^{-10} dB/m, and 1.87×10^{-4} dB/m, respectively. Although the losses for the three modes at λ_F are much lower than those at λ_E, they are still higher than their respective values of $CL_{\min}$. The further reduction of modal losses at λ_F can be achieved by increasing Λ. However, the red-shift of OPBG induced by increasing Λ may result in the fluorescence band partly moving outside of the OPBG range, which would reduce the fluorescence capture efficiency. Thus, for the maximum fluorescence signal detected by the PD or OSA, we should make a tradeoff between enhancing capture efficiency and reducing transmission loss by optimizing the value of Λ.

The design strategy of D-HCBFs for fluorescence sensing is as follows: First, the setting of the initial Λ_i is the same as that for the C-HCBF design mentioned above. Second, check whether λ_E is outside of the PBG range at normal incidence for both TE and TM waves. If the criterion is satisfied, Λ_i can be set as the final value of Λ. If not, the rule of PBG structure scaling up with Λ is used to finely adjust Λ_i until the criterion is satisfied. Finally, the parameters of the defect layer are determined by the agreement of central wavelengths for the loss peak and excitation light. As mentioned above, λ_{MP} of the fundamental HE_{11} mode should be identical to λ_{SP}, so that all the surviving guided modes including pure TE and TM modes and mixed modes can have the maximum losses at the same wavelength. However, it is extremely difficult to ensure that λ_F is within the OPBG range and simultaneously ensure that λ_E is in accordance with both λ_{MP} and λ_{SP}. In particular, the red-shifts of λ_{MP} and λ_{SP} induced by material dispersion are not the same, which results in an increased difficulty of satisfying the matching requirement of $\lambda_{MP} = \lambda_{SP}$. Accordingly, in the practical fiber design, the parameter setting for the defect layer is mainly concerned with the agreement between λ_{MP} and λ_E, while λ_{SP} should be as close to λ_E as possible. This approach can enable most guided modes (except for pure TE modes) to be filtered due to high transmission losses.

As demonstrated experimentally in [38], the rhodamine 6G solution is excited by an LD pumped solid-state laser with the central wavelength of 532 nm, resulting in the fluorescence with the central wavelength of 556 nm. The interval between excitation and fluorescence wavelengths is so small that the PBG effect cannot serve for filtering the residual excitation light mixed with fluorescence. Thus, we demonstrate a designed D-HCBF with $d_c = 200$ μm, $\Lambda = 151$ nm, $t_d = 2t_l$, $N_d = 9$, and

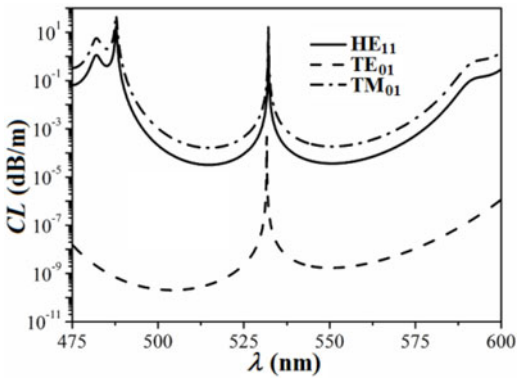

Fig. 11. Loss spectra of HE_{11}, TE_{01}, and TM_{01} modes in the designed D-HCBF with $d_c = 200$ μm, $\Lambda =$ 151 nm, $t_d = 2t_l$, $N_d = 9$, and $N = 20$.

$N = 20$, in which the loss spectra of the HE_{11}, TE_{01} and TM_{01} modes are shown in Fig. 11. It can be seen that both the HE_{11} and TM_{01} modes have the same loss peak at 532.1 nm, slightly differing from that at 531.6 nm for the TE_{01} mode. The fluorescence wavelength of 556 nm falls well within the OPBG ranging from 538 to 577 nm. Accordingly, we can conclude that the designed D-HCBF is suitable for the targeted fluorescence sensing. We note that the filtering ability is sufficient in the D-HCBF-based fluorescence sensing scheme using LD as the excitation source. However, it would be restricted in the sensing scheme using broadband LED, because the narrow bandwidth of loss peak in the D-HCBF might not cover the wide excitation spectrum.

In general, as the key element of our proposed scheme, the multifunctional HCBFs tend to be designed for a specific sensing case. Otherwise, the performance of the HCBF-based fluorescence sensing scheme would be reduced. However, both the PBG structure and modal loss characteristic of HCBFs can be adjusted via multiple degrees of freedom, including n_h, n_l, n_d, d_c, t_h, t_l, t_d, N_d, and N, which will provide sufficient opportunities to design the desirable HCBFs. According to the current fabrication ability [30], the designed HCBFs can be easily available after the determination of suitable parameters.

6. Conclusion

We have proposed a compact fluorescence sensing scheme using C-HCBF or D-HCBF as a sample cell, a collector, and a delivery channel for the desired fluorescence, and a filter for the residual excitation light mixed with fluorescence. The excitation light with wavelength outside of the PBG range at normal incidence can stimulate samples through the multilayer cladding of HCBFs. For the enhancement of capture efficiency, the fluorescence wavelength should fall within their OPBG range. The residual excitation light mixed with fluorescence can be filtered by using the PBG effect in C-HCBFs and the TR behavior in D-HCBFs. The relationship between the defect layer and modal loss characteristics in D-HCBFs are discussed in detail, which determining the filtering performance for improving the SNR. Additionally, the influences of material dispersion on the PBG structure and modal characteristics are considered in the practical design of HCBFs. Accordingly, the design strategies of C-HCBF and D-HCBF for fluorescence sensing are presented, respectively. Finally, we demonstrated two typical design examples to confirm the feasibility of our proposed fluorescence sensing scheme.

Acknowledgment

The authors would like to thank the anonymous reviewers for their valuable suggestions.

References

[1] X. Fan and I. M. White, "Optofluidic microsystems for chemical and biological analysis," *Nature Photon.*, vol. 5, no. 10, pp. 591–597, Sep. 2011.
[2] J. Karolin and C. Geddes, "Spectral shifts in metal-enhanced fluorescence," *Appl. Phys. Lett.*, vol. 105, no. 6, Aug. 2014, Art. no. 063102.
[3] X. Geng, D. Wu, and Y. Guan, "A compact and highly sensitive light-emitting diode-induced fluorescence detector for capillary flow systems," *Talanta*, vol. 88, pp. 463–467, Jan. 2012.
[4] Y. Xin, Q. Wang, T. Liu, L. Wang, J. Li, and Y. Fang, "A portable and autonomous multichannel fluorescence detector for on-line and in situ explosive detection in aqueous phase," *Lab Chip*, vol. 12, no. 22, pp. 4821–4828, Sep. 2012.
[5] X. Yang, T. Yuan, G. Yue, E. Li, and L. Yuan, "Optofluidic integrated in-fiber fluorescence online optical fiber sensor," *Sens. Actuators B*, vol. 215, pp. 345–349, Aug. 2015.
[6] J. Xu, B. Yang, H. Tian, and Y. Guan, "A windowless flow cell-based miniaturized fluorescence detector for capillary flow systems," *Anal. Bioanal. Chem.*, vol. 384, no. 7, pp. 1590–1593, Apr. 2006.
[7] P. Ghenuche, H. Rigneault, and J. Wenger, "Hollow-core photonic crystal fiber probe for remote fluorescence sensing with single molecule sensitivity," *Opt. Exp.*, vol. 20, no. 27, pp. 28379–28387, Dec. 2012.
[8] Y. Huang, Y. Xu, and A. Yariv, "Fabrication of functional microstructured optical fibers through a selective-filling technique," *Appl. Phys. Lett.*, vol. 85, no. 22, pp. 5182–5184, Dec. 2004.
[9] J. B. Jensen *et al.*, "Photonic crystal fiber based evanescent-wave sensor for detection of biomolecules in aqueous solutions," *Opt. Lett.*, vol. 29, no. 17, pp. 1974–1976, Sep. 2004.
[10] S. O. Konorov, A. M. Zheltikov, and M. Scalora, "Photonic-crystal fiber as a multifunctional optical sensor and sample collector," *Opt. Exp.*, vol. 13, no. 9, pp. 3454–3459, May 2005.
[11] J. B. Jensen, P. E. Hoiby, G. Emiliyanov, O. Bang, L. H. Pedersen, and A. Bjarklev, "Selective detection of antibodies in microstructured polymer optical fibers," *Opt. Exp.*, vol. 13, no. 15, pp. 5883–5889, Jul. 2005.
[12] S. Smolka, M. Barth, and O. Benson, "Highly efficient fluorescence sensing with hollow core photonic crystal fibers," *Opt. Exp.*, vol. 15, no. 20, pp. 12783–12791, Oct. 2007.
[13] V. S. Afshar, S. C. Warren-Smith, and T. M. Monro, "Enhancement of fluorescence-based sensing using microstructured optical fibres," *Opt. Exp.*, vol. 15, no. 26, pp. 17891–17901, Dec. 2007.
[14] Q. Li, K. J. Morris, P. K. Dasgupta, I. M. Raimundo, Jr., and H. Temkin, "Portable flow-injection analyzer with liquid-core waveguide based fluorescence, luminescence, and log path length absorbance detector," *Analytica Chim. Acta*, vol. 479, no. 2, pp. 151–165, Mar. 2003.
[15] T. Okada, "Liquid-core waveguide in CE," *Electrophoresis*, vol. 28, no. 19, pp. 3414–3419, Sep. 2007.
[16] B. Temelkuran, S. D. Hart, G. Benoit, J. D. Joannopoulos, and Y. Fink, "Wavelength-scalable hollow optical fibres with large photonic bandgaps for CO2 laser transmission," *Nature*, vol. 420, pp. 650–653, Dec. 2002.
[17] Y. Fink *et al.*, "A dielectric omnidirectional reflector," *Science*, vol. 282, pp. 1679–1682, Nov. 1998.
[18] C. Charlton, B. Temelkuran, G. Dellemann, and B. Mizaikoff, "Midinfrared sensors meet nanotechnology: Trace gas sensing with quantum cascade lasers inside photonic bang-gap hollow waveguides," *Appl. Phys. Lett.*, vol. 86, no. 19, May 2005, Art. no. 194102.
[19] K. J. Rowland, S. Afshar, A. Stolyarov, Y. Fink, and T. M. Monro, "Bragg waveguides with low-index liquid cores," *Opt. Exp.*, vol. 20, no. 1, pp. 48–62, Jan. 2011.
[20] D. Passaro *et al.*, "All-silica hollow-core microstructured Bragg fibers for biosensor application," *IEEE Sens. J.*, vol. 8, no, 7, pp. 1280–1286, Jul. 2011.
[21] A. Yildirim, M. Vural, M. Yaman, and M. Bayindir, "Bioinspired optoelectronic nose with nanostructured wavelength-scalable hollow-core infrared fibers," *Adv. Mater.*, vol. 23, no. 10, pp. 1263–1267, Mar. 2011.
[22] A. M. Stolyarov *et al.*, "Enhanced chemiluminescent detection scheme for trace vapor sensing in pneumatically-tuned hollow core photonic bandgap fibers," *Opt. Exp.*, vol. 20, no. 11, pp. 12407–12415, May 2012.
[23] H. Qu and M. Skorobogatiy, "Resonant bio- and chemical sensors using low-refractive-index-contrast liquid-core Bragg fibers," *Sens. Actuators B*, vol. 161, no. 1, pp. 261–268, Jan. 2012.
[24] T. Monti and G. Gradoni, "Hollow-core coaxial fiber sensor for biophotonic detection," *IEEE J. Sel. Top. Quant. Electron.*, vol. 20, no. 2, Mar. 2014, Art. no. p. 6900409.
[25] J. Li, H. Qu, and M. Skorobogatiy, "Simultaneous monitoring the real and imaginary parts of the analyte refractive index using liquid-core photonic bandgap Bragg fibers," *Opt. Exp.*, vol. 23, no. 18, pp. 22963–22976, Sep. 2015.
[26] J. Li, H. Qu, and M. Skorobogatiy, "Squeezed hollow-core photonic Bragg fiber for surface sensing applications," *Opt. Exp.,* vol. 24, no. 14, pp. 15687–15701, Jul. 2016.
[27] D. Chen, T. Yang, J. Wu, L. Shen, K. Liao, and S. He, "Band-rejection fiber filter and fiber sensor based on a Bragg fiber of transversal resonant structure," *Opt. Exp.*, vol. 16, no. 21, pp. 16489–16495, Oct. 2008.
[28] A. Argyros, M. A. Van Eijkelenborg, M. C. J. Large, and I. M. Bassett, "Hollow-core microstructured polymer optical fiber," *Opt. Lett.*, vol. 31, no. 2, pp. 172–174, Jan. 2006.
[29] S. G. Johnson *et al.*, "Low-loss asymptotically single-mode propagation in large-core omniguide fibers," *Opt. Exp.*, vol. 9, no. 13, pp. 748–779, Dec. 2001.
[30] O. Shapira *et al.*, "Surface-emitting fiber lasers," *Opt. Exp.*, vol. 14, no. 9, pp. 3929–3935, May 2006.
[31] T. D. Engeness *et al.*, "Dispersion tailoring and compensation by modal interactions in Omniguide fibers," *Opt. Exp.*, vol. 11, no. 10, pp. 1175–1196, May 2003.
[32] C. Lin, W. Zhang, Y. Huang, and J. Peng, "Defect Bragg fiber with low loss for broadband and zero dispersion slow light," *J. Lightw. Technol.*, vol. 25, no. 12, pp. 3776–3783, Dec. 2007.
[33] L. Shang, X. Yang, Y. Xia, and H. Wang, "Hollow core Bragg fibers with a heterostructured cladding based on ternary one-dimensional photonic crystal for mid-infrared broadband and low-loss transmission," *J. Lightw. Technol.*, vol. 32, no. 9, pp. 1717–1725, May 2014.

[34] Y. H. Lu *et al.*, "Fabrication and analysis of one-dimensional defect-induced ultrawide photonic band gaps," *J. Appl. Phys.*, vol. 101, no. 10, May 2007, Art. no. 103103.
[35] L. Shang, Z. Huang, and Y. Liao, "Comparative study of guided modes in hollow core Bragg fibers with binary and ternary photonic bandgap claddings," *J. Opt. Soc. Amer. B*, vol. 32, no. 6, pp. 1155–1164, Jun. 2015.
[36] M. Miyagi, "Waveguide-loss evaluation in circular hollow waveguides and its ray-optical treatment," *J. Lightw. Technol.*, vol. LT-3, no. 2, pp. 303–307, Apr. 1985.
[37] H. Ko, J. Nah, K. W. Paik, and Y. Park, "Effects of the polymer residues on via contact resistance after reactive ion etching," *J. Vac. Sci. Technol. B*, vol. 20, no. 3, pp. 1000–1007, May/Jun. 2002.
[38] C. A. Guyer and S. Tao, "Total internal reflection fluorescence spectrometry using a dual optical fiber sample cell," *Appl. Spectrosc.*, vol. 69, no. 5, pp. 608–612, May 2015.